A RANKL-UCHL1-sCD13 negative feedback loop limits osteoclastogenesis in subchondral bone to prevent osteoarthritis progression

Wenquan Liang [1,2,12] ✉, Ru Feng [3,4,5,12], Xiaojia Li [3,12], Xingwei Duan [1,12], Shourui Feng[6], Jun Chen[7], Yicheng Li[3], Junqi Chen[3], Zezheng Liu[8], Xiaogang Wang[8], Guangfeng Ruan[9], Su'an Tang[10], Changhai Ding [10], Bin Huang [8] ✉, Zhipeng Zou [1] ✉ & Tianyu Chen [8,11] ✉

Abnormal subchondral bone remodeling plays a pivotal role in the progression of osteoarthritis (OA). Here, we analyzed subchondral bone samples from OA patients and observed a significant upregulation of ubiquitin carboxy-terminal hydrolase L1 (UCHL1) specifically in subchondral bone osteoclasts. Notably, we found a strong correlation between UCHL1 expression and osteoclast activity in the subchondral bone during OA progression in both human and murine models. Conditional UCHL1 deletion in osteoclast precursors exacerbated OA progression, while its overexpression, mediated by adeno-associated virus 9, alleviated this process in male mice. Mechanistically, RANKL stimulates UCHL1 expression in osteoclast precursors, subsequently stabilizing CD13, augmenting soluble CD13 (sCD13) release, and triggering an autocrine inhibitory effect on the MAPK pathway, thereby suppressing osteoclast formation. These findings unveil a previously unidentified negative feedback loop, RANKL-UCHL1-sCD13, that modulates osteoclast formation and presents a potential therapeutic target for OA.

Osteoarthritis (OA) is a common and disabling condition that causes joint pain and stiffness, impacting about 300 million individuals worldwide[1,2]. Unfortunately, there are currently no drugs available that can effectively halt the progression of OA and prevent long-term disability[3]. With the increasing aging and obesity of the population worldwide, the incidence of OA is rising[4]. Consequently, an urgent clinical demand exists to develop innovative disease-modifying drugs or regenerative therapies for OA.

OA is a whole joint disease characterized by progressive degradation of articular cartilage, subchondral bone structural changes,

[1]Department of Cell Biology, School of Basic Medical Sciences, Southern Medical University, Guangzhou, China. [2]Department of Anatomy, School of Basic Medical Sciences, Southern Medical University, Guangzhou, China. [3]Department of Rehabilitation medicine, The Third Affiliated Hospital of Southern Medical University, Guangzhou, China. [4]School of Rehabilitation, Capital Medical University, Beijing, China. [5]Department of Spinal and Neural Functional Reconstruction, China Rehabilitation Research Center, Beijing, China. [6]State Key Laboratory of Biocontrol and Guangdong Provincial Key Laboratory of Plant Resources, School of Life Sciences, Sun Yat-sen University, Guangzhou, China. [7]Department of Rehabilitation Medicine, Nanfang Hospital of Southern Medical University, Guangzhou, China. [8]Department of Orthopaedics, The Third Affiliated Hospital of Southern Medical University, Guangzhou, China. [9]Clinical Research Centre, Guangzhou First People's Hospital, Guangzhou, China. [10]Clinical Research Centre, Zhujiang Hospital, Southern Medical University, Guangzhou, China. [11]Department of Orthopaedic Surgery, Third Hospital of Hebei Medical University, Shijiazhuang, China. [12]These authors contributed equally: Wenquan Liang, Ru Feng, Xiaojia Li, Xingwei Duan. ✉e-mail: liangwqycy@163.com; binxue483@163.com; zzp@smu.edu.cn; nysycty@163.com

osteophytes formation, joint inflammation, and impaired function[5]. Chondrocytes, the sole cell type in articular cartilage, play a crucial role in maintaining the structure and function of cartilage[6]. In OA, there is an imbalance in the metabolism of the cartilage extracellular matrix, resulting in the loss of essential components like collagen and proteoglycans, leading to cartilage thinning and structural damage[7]. The synovial tissue that lines the joint cavity is affected in OA, with synoviocytes proliferating, macrophages polarizing towards an inflammatory state[8], releasing inflammatory mediators and enzymes that contribute to cartilage degradation and osteophyte formation. Osteocytes, the most abundant type of bone cells, have been reported to play a significant role in the homeostasis of subchondral bone and cartilage, as well as joint diseases[9,10].

Recent studies have emphasized the significant role of abnormal subchondral bone remodeling in cartilage deterioration[11–13]. In a healthy joint, the articular cartilage and subchondral bone cooperate as a functional unit, with pressure transmission from the cartilage to the underlying subchondral bone. However, unstable mechanical loading contributes to increased recruitment of osteoclasts, resulting in abnormal subchondral bone remodeling. Furthermore, subchondral bone osteoclasts are associated with OA pain as they can regulate sensory innervation[14]. Both preclinical studies and clinical trials have indicated the favorable effects of inhibiting osteoclast function with bisphosphonates, denosumab or MIV-711, a cathepsin K inhibitor, on OA[15–23]. Hence, targeting osteoclastic resorption in subchondral bone holds great potential for treating OA.

Posttranslational modifications, including ubiquitination, are pivotal in regulating protein stability, distribution, and function. Ubiquitination is a reversible process, and facilitated by deubiquitinating enzymes (DUBs), also known as deubiquitinases[24]. Ubiquitin carboxy-terminal hydrolase L1 (UCHL1), also referred to as PGP9.5, belongs to the small family of ubiquitin C-terminal hydrolases and serves as a DUB. Dysregulation of UCHL1 is closely associated with neurodegenerative diseases, tumors, glomerulonephritis, and cardiovascular diseases[25–27]. Mouse models with UCHL1 mutations have been described, whereby the *gad* mice exhibit neurologic phenotype and decreased bone mineral density (BMD)[28]. Moreover, recent studies have highlighted the significance of UCHL1 in osteoporosis[29,30]. However, the precise role of UCHL1 in subchondral bone remodeling and the pathogenesis of OA remains unclear. Here, we show that UCHL1 is involved in a previously unidentified negative feedback loop, RANKL-UCHL1-sCD13, that limits osteoclastogenesis. Deletion of UCHL1 in osteoclast precursor cells enhances subchondral osteoclastogenesis and OA progression, while overexpression of UCHL1 through adeno-associated virus serotype 9 alleviates this process. Thus, targeting UCHL1 could represent a potential therapeutic strategy for alleviating OA.

Results

The upregulation of UCHL1 correlates with elevated osteoclast activity in subchondral bone in humans and mice with OA

To explore the role of DUBs in subchondral bone pathology in OA, we performed a PCR array analysis of 90 DUB genes in OA subchondral bone samples, yielding differential expression of 6 significantly upregulated and 5 significantly downregulated DUBs (Fig. 1a–c). Among the upregulated DUBs, the most notable change was observed in UCHL1 and confirmed by qPCR and western blotting (Fig. 1d, e). Furthermore, UCHL1 was specifically expressed in CTSK-positive osteoclasts (Fig. 1f and Supplementary Fig. 1a), with an increased presence of UCHL1-positive osteoclasts in regions of subchondral osteoarthritis in humans (Fig. 1f, g).

Next, we investigated the association between UCHL1 expression and osteoclast activity in the surgical destabilization of the medial meniscus (DMM) surgery induced posttraumatic OA mice model at different time periods (Supplementary Fig. 1b–g). The articular cartilage degenerated significantly by 4 weeks according to the higher OA Research Society International (OARSI) grade, with continued progression at 8 weeks (Supplementary Fig. 1d, e). However, the number of TRAP-positive osteoclasts peaked at 2 weeks and declined thereafter (Fig. 1h, i). Consistent with this observation, subchondral bone mass and subchondral bone plate thickness were significantly reduced at 2 weeks (Supplementary Fig. 1f, g). Immunofluorescence analysis revealed that the number of UCHL1-positive osteoclasts in subchondral bone reached its peak at 2 weeks after DMM and returned to baseline by 8 weeks (Fig. 1j, k). These results demonstrated a strong correlation between increased UCHL1 expression, elevated osteoclast activity, subchondral bone deterioration, and subsequent cartilage degeneration during OA progression.

UCHL1 inhibits osteoclastogenesis in vitro

In the presence of macrophage colony-stimulating factor (M-CSF) and receptor activator of NF-κB ligand (RANKL), BMMs differentiate into multinucleated, TRAP-positive osteoclasts within a 4–5-day culture period. We induced BMMs to differentiate into osteoclasts at different time periods, and then detected the expression of UCHL1. The upregulation of UCHL1 mRNA expression during osteoclastogenesis was confirmed by qPCR and along with other well-known osteoclast maturation makers such as Acp5 and Ctsk (Fig. 2a). Similarly, at the protein level, UCHL1 content increased as BMMs were induced to form osteoclasts (Fig. 2b).

To further elucidate the function of UCHL1 in osteoclastogenesis, LysM-Cre;UCHL1^{fl/fl} mice (cKO mice) were generated, resulting in diminished UCHL1 expression in all myeloid lineage cells including BMMs (osteoclast precursor cells) (Supplementary Fig. 2a–g). In vitro cultures of BMMs from WT and cKO mice showed that UCHL1 deficiency led to a notable increase in osteoclastogenesis, as indicated by higher levels of transcripts and proteins associated with differentiation (c-fos and Nfatc1), fusion (Dc-stamp, Oc-stamp, and Atp6v0d2), and function (Ctsk and Acp5) markers (Fig. 2c, d). Consistent with these findings, UCHL1 knockout resulted in increased osteoclast numbers and resorption activity (Fig. 2e, f). Treatment with LDN-57444, a selective UCHL1 inhibitor, also resulted in an increase in the number and size of TRAP-positive multinucleated osteoclasts (Supplementary Fig. 3a, b). Additionally, the absence of UCHL1 had minimal impact on BMMs proliferation, as indicated by EdU staining (Fig. 2g). Collectively, these results demonstrate that intrinsic loss of UCHL1 leads to enhanced osteoclastogenesis and function.

UCHL1 deletion in osteoclasts exacerbates DMM-induced OA progression in a mouse model

Next, we examined the role of UCHL1 in OA pathogenesis by employing UCHL1 cKO mice. Upon normal diet, adult cKO and WT mice (3-months-old) displayed no significant difference in bone phenotypes (Supplementary Fig. 4a–d). Subsequently, DMM surgery was performed on 3-month-old WT and cKO mice (Fig. 3a and Supplementary Fig. 5a, b). Two weeks after the sham surgery, there were no notable distinctions in the number of TRAP-positive osteoclasts between the two groups. However, the subchondral bone of UCHL1 cKO mice exhibited nearly two-fold higher levels of TRAP-positive osteoclasts compared to the WT group at the 2-week post DMM surgery (Fig. 3b, c). Concurrently, micro-CT analysis confirmed an evident reduction in bone volume and subchondral bone plate thickness in the subchondral bone of UCHL1 cKO mice (Fig. 3d, e), consistent with the increase in osteoclasts.

Safranin-O/Fast Green staining revealed that DMM-induced cartilage degeneration was more severe in UCHL1 cKO mice compared to WT mice at 8 weeks after DMM surgery, as demonstrated by higher OARSI grades (Fig. 3f, g). Immunohistochemical staining further indicated that UCHL1 knockout in
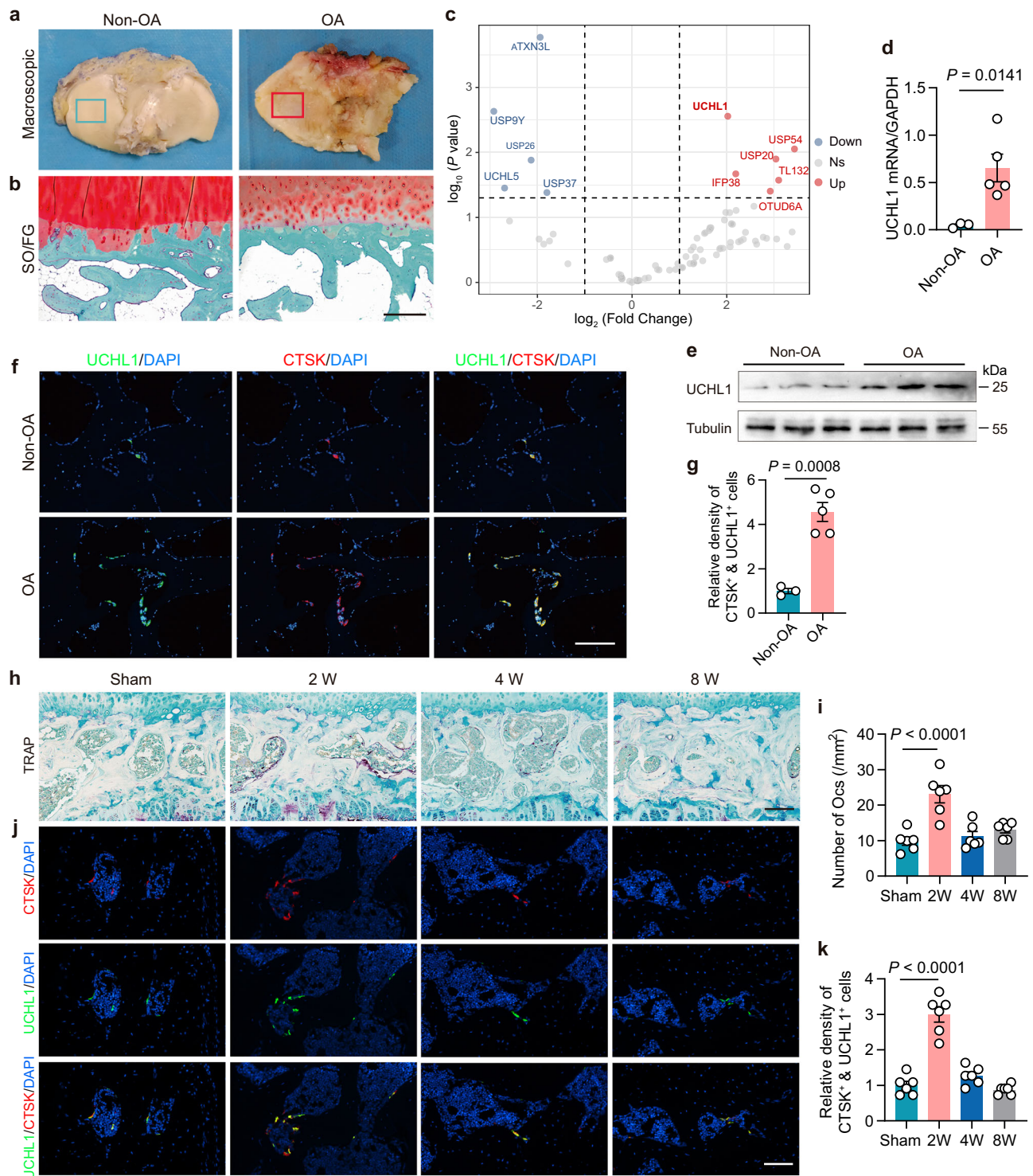
Fig. 1 | UCHL1 upregulation associates with increased osteoclast activity in subchondral bone in human and mice with OA. a Macroscopic images of tibia plateaus from OA patients and non-OA donors. **b** Safranin-O/fast green (SO/FG) staining of sagittal sections of the subchondral tibia in the OA patients and non-OA donors; showing proteoglycan (red) and bone (green). This experiment was repeated three times independently with similar results. Scale bar: 500 μm. **c** Volcano plot of PCR array analysis, demonstrating differentially expressed deubiquitinase genes in subchondral bone of 3 OA patients and 3 non-OA donors (fold-change >2, $p < 0.05$). Statistical analysis was performed using two-tailed unpaired Student's t-test. High and low expression are denoted by red and blue, respectively. **d, e** mRNA and protein expression of UCHL1 in subchondral bone of OA patients and non-OA donors. $n = 3, 5$ individuals. **f** Immunofluorescence staining of CTSK and

UCHL1 in subchondral bone of OA patients and non-OA donors. Scale bar: 200 μm. **g** Quantitative analysis of CTSK and UCHL1 double-positive cell intensity in subchondral bone of 3 OA patients and 5 non-OA donors. **h** TRAP staining of tibial subchondral bone (coronal view) at different time points after DMM surgery. Scale bar: 100 μm. **i** Quantitative analysis of TRAP-positive osteoclast density in subchondral bone ($n = 6$ mice per group). **j** Immunofluorescence staining of CTSK and UCHL1 in subchondral bone at different time points after DMM surgery. Scale bar: 100 μm. **k** Quantitative analysis of CTSK and UCHL1 double-positive cell intensity ($n = 6$ mice per group). All data are presented as mean ± SEM. Statistical analyzes utilized two-tailed unpaired Student's t-test (**c, d, g**) and ANOVA with Tukey post hoc test for pairwise comparisons (**i, k**). OA, osteoarthritis; SO/FG, Safranin-O/fast green. Source data are provided as a Source Data file.
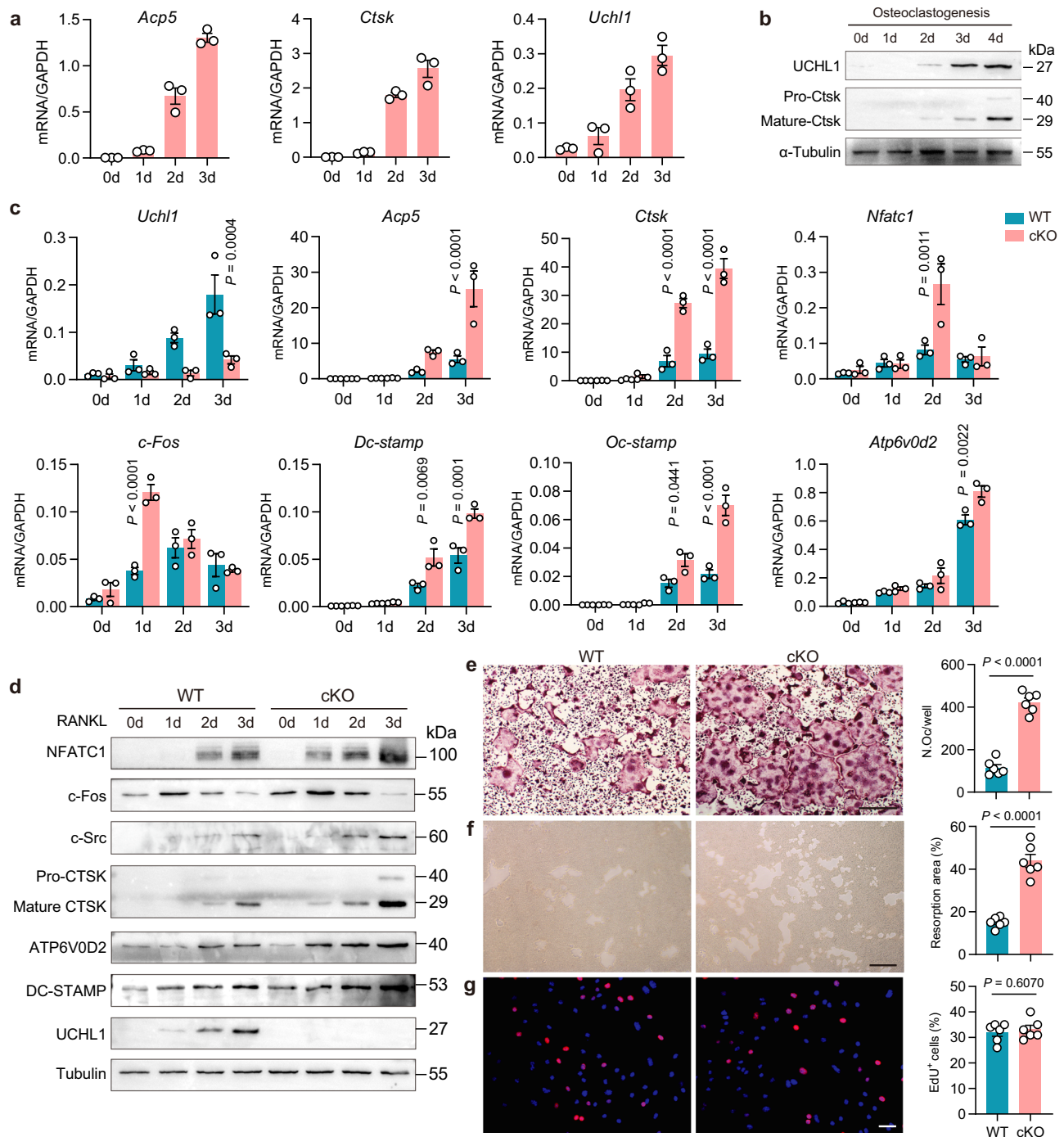
Fig. 2 | UCHL1 inhibits osteoclastogenesis in vitro. a, b Ctsk, Acp5 and Uchl1 expression in BMMs during RANKL and M-CSF induced osteoclastogenesis ($n = 3$ independent cultures). **c, d** qPCR and immunoblot analysis of osteoclastogenic markers in WT and cKO BMMs cultured with RANKL and M-CSF ($n = 3$ independent cultures). **e** TRAP staining and quantitative analysis of BMMs from WT and cKO mice after 4 days of RANKL and M-CSF induction ($n = 6$ independent cultures). Scale bar: 500 μm. **f** Resorption analysis of BMMs from WT and cKO mice after 10 days of RANKL and M-CSF induction ($n = 6$ independent cultures). Scale bar: 200 μm. **g** EdU proliferation assay in BMMs from WT and cKO mice ($n = 6$ independent cultures). Scale bar: 50 μm. All data are presented as mean ± SEM. Statistical analysis employed two-tailed unpaired Student's t-test (**e, f, g**) and two-way ANOVA with Tukey post hoc test for pairwise comparisons (**c**). Source data are provided as a Source Data file.

osteoclasts led to a decrease in the expression of anabolic marker type II collagen and an increase in the expression of catabolic marker MMP13 in the knee articular cartilage of mice (Fig. 3h, i). Additionally, at 8 weeks after DMM, cKO mice exhibited heightened sensitivity to pain (Fig. 3j). Collectively, these findings suggest that UCHL1 deletion in BMMs exacerbates OA progression by promoting osteoclast activity.

UCHL1 interacts with CD13 and promotes CD13 protein stability through deubiquitination

UCHL1 is a DUB enzyme responsible for preventing protein degradation by removing ubiquitin from substrate proteins. Our proposed criteria for the substrate of UCHL1 necessitated two conditions: (1) interaction with UCHL1 and (2) decreased protein levels of the substrate upon UCHL1 knockout. Initially, proteomics analysis was
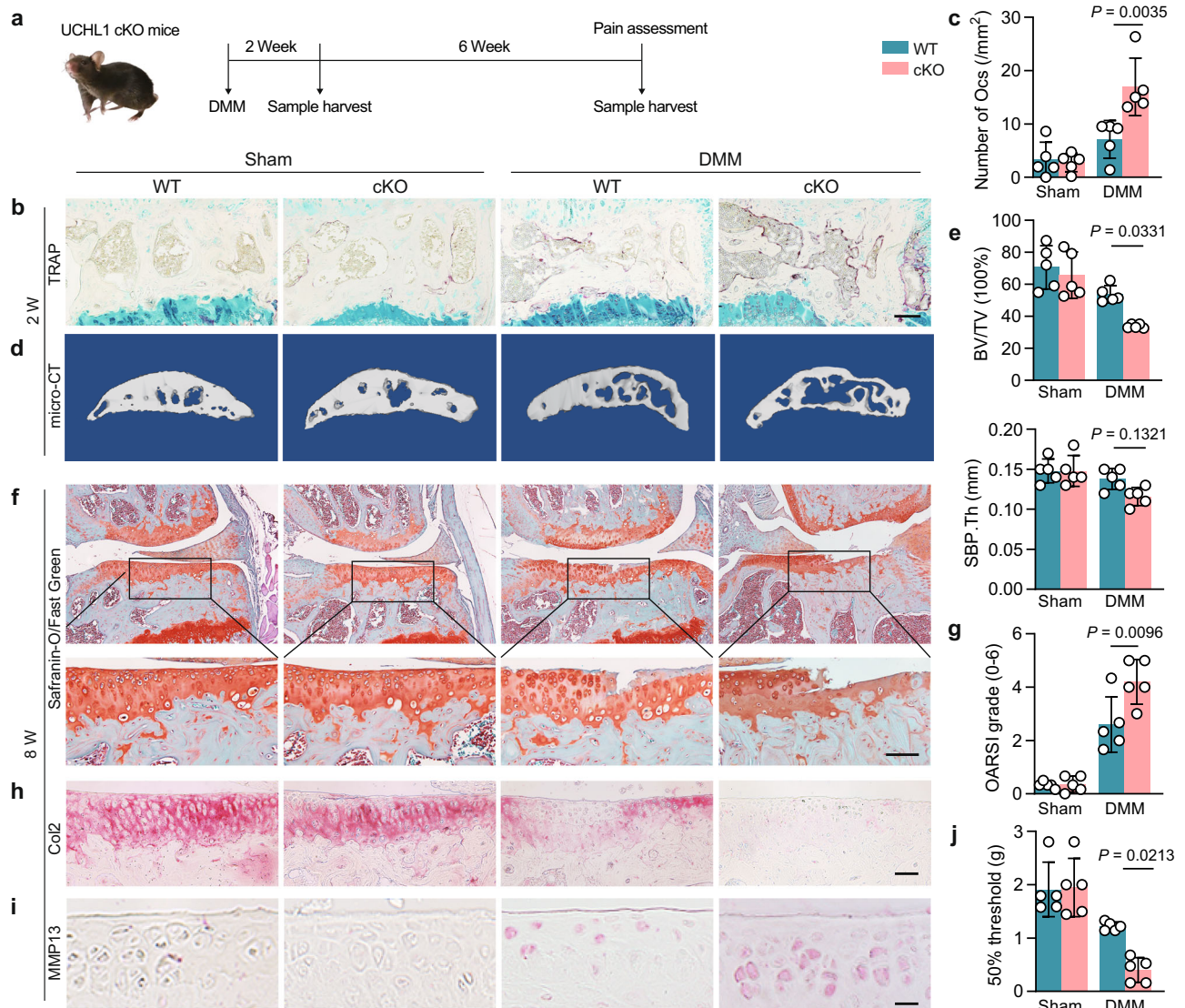
Fig. 3 | UCHL1 deletion in osteoclasts exacerbates DMM-induced OA progression in a mouse model. a Experimental design schematic of DMM surgery in WT and cKO mice. **b** TRAP staining of the tibia subchondral bone (coronal view) 2 weeks after DMM surgery. Scale bar: 100 μm. **c** Quantitative analysis of TRAP-positive osteoclast density in subchondral bone ($n = 5$ mice per group). **d** 3D micro-CT images of the tibial subchondral bone medial compartment 2 weeks after DMM surgery. **e** Quantitative analysis of subchondral bone mass (BV/TV) and subchondral bone plate thickness (SBP.Th) ($n = 5$ mice per group). **f** Safranin-O/fast green staining of the tibial subchondral bone (coronal view) 8 weeks after DMM surgery. Scale bar: 100 μm. **g** OARSI grade of the tibial articular cartilage ($n = 5$ mice per group). **h** Representative images of Col2 immunohistochemistry in tibial articular cartilage at 8 weeks after DMM. Scale bar: 50 μm. **i** Representative images of MMP13 immunohistochemistry in tibial articular cartilage at 8 weeks after DMM. Scale bar: 20 μm. **j** Paw withdrawal threshold measured in the right hind paw at 8 weeks after DMM ($n = 5$ mice per group). All data are presented as mean ± SEM. Statistical analysis utilized two-way ANOVA with Tukey post hoc test for pairwise comparisons (**c**, **e**, **g**, **j**). The experiments in **h**, **i** were independently repeated five times with similar results. DMM, destabilized medial meniscus; OARSI, Osteoarthritis Research Society International; BV/TV, bone volume/total volume; SBP.Th, subchondral bone plate thickness. Source data are provided as a Source Data file.

conducted on cultured BMMs from WT and cKO mice (Supplementary Fig. 6a, b and Supplementary Data 1). Differential expression analysis identified 502 upregulated differentially expressed proteins (DEPs) and 263 downregulated DEPs (fold change >1.2 and p-value < 0.05) (Fig. 4a and Supplementary Data 2). Subsequently, KEGG and GO enrichment analysis determined that these DEPs were enriched in processes related to osteoclast differentiation, bone resorption, and bone remodeling (Supplementary Fig. 6c, d). Notably, expression of proteins associated with osteoclast functions, such as Acp5, Ctsk, and Nfatc1, was upregulated in cKO BMMs, while proteins inhibiting osteoclast differentiation, such as Fcgr4 and Itgb5, were down-regulated (Fig. 4b). These findings provide additional evidence supporting the inhibitory effect of UCHL1 on osteoclastogenesis.

Based on the aforementioned criteria, a comparison was made between the downregulated proteins and interacting proteins from the immunoprecipitation experiment (Supplementary Data 3). Three candidate substrates, namely C1qa, C1qc, and CD13, were identified (Fig. 4c). It is worth noting that C1qa, C1qb, and C1qc collectively form the 18 subunits of complement component C1q[31]. To validate these candidates, western blot analysis was performed on C1qa and CD13, revealing a significant reduction in CD13 protein content in UCHL1 knockout BMMs, while C1qa displayed a mild decrease (Fig. 4d). Furthermore, UCHL1 was found to regulate CD13 expression solely at the protein level, rather than at the mRNA level (Fig. 4e), suggesting that UCHL1 affects the posttranslational modification of CD13.
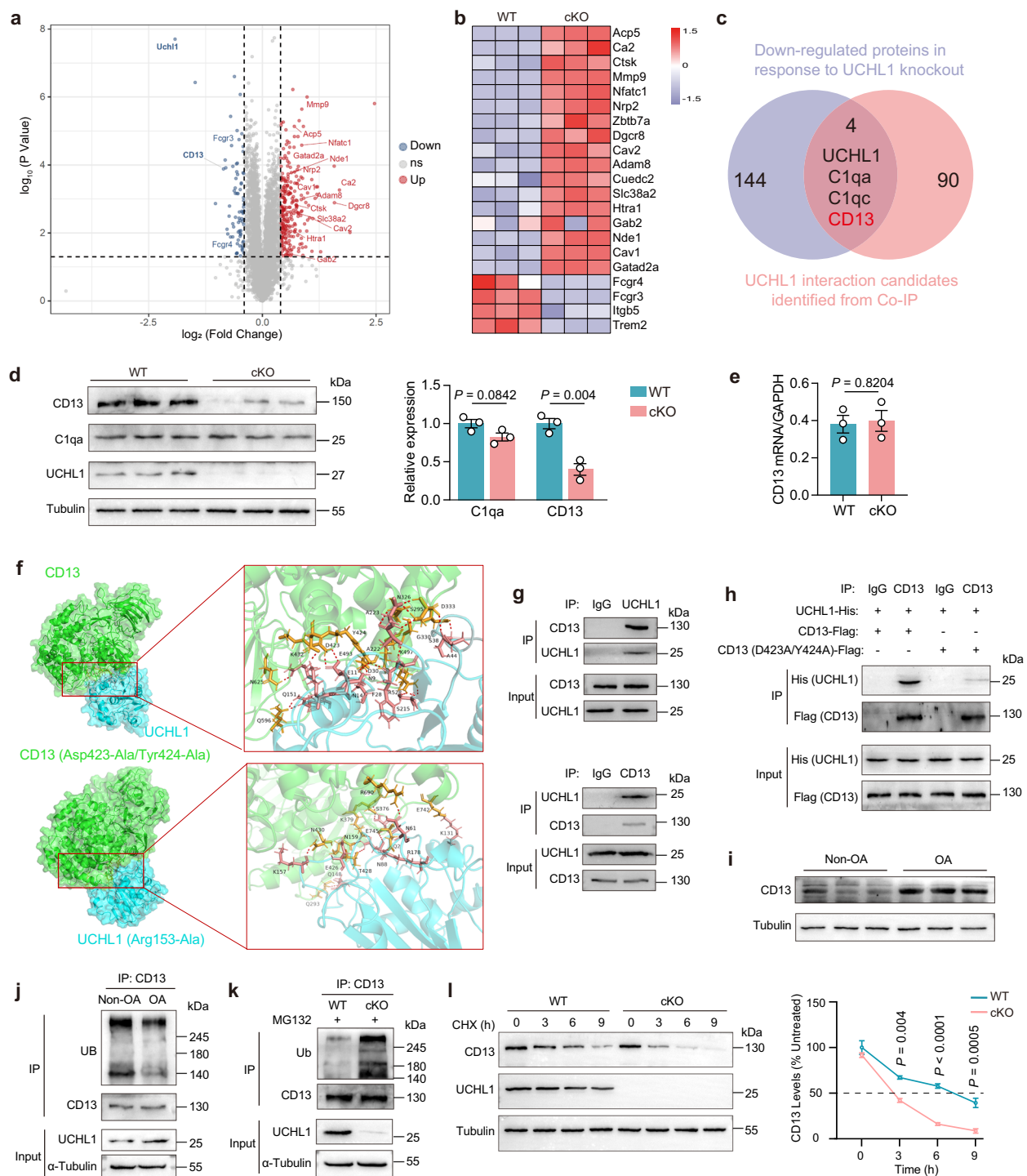
Fig. 4 | UCHL1 interacts with CD13 and promotes CD13 protein stability through deubiquitination in preosteoclasts. a Volcano plot illustrating the differential expression of proteins (DEPs) in BMMs from WT and cKO mice. Statistical analysis was performed using two-tailed unpaired Student's t-test. DEPs increased by UCHL1 knockout are shown in red, while those decreased are denoted in blue. **b** Heat map presenting the DEPs associated with osteoclast function. **c** Strategy employed for the identification of substrate proteins, where downregulated proteins were compared with interacting proteins from the immunoprecipitation experiment. **d** Immunoblot and statistical analysis of CD13 and C1qa in BMMs from WT and cKO mice (n = 3 independent cultures). **e** Quantitative real-time PCR analysis of CD13 in BMMs from WT and cKO mice (n = 3 independent cultures). **f** Molecular docking model illustrating the interactions between wild-type UCHL1 and CD13 protein, as well as their respective mutants. Amino acids contributing to hydrogen bonds from UCHL1 (pink) and CD13 (brown) are denoted in one-letter code followed by their position in each chain. UCHL1 is depicted with a blue surface, while CD13 is illustrated with a green surface. **g** Co-immunoprecipitation of UCHL1 and CD13 in BMMs. **h** Co-immunoprecipitation of wild-type UCHL1 and mutated CD13 (D423A/Y424A) in BMMs. **i** Protein expression of CD13 in subchondral bone of 3 OA patients and 3 non-OA donors. **j** Ubiquitination of CD13 protein in subchondral bone of OA patients and non-OA donors. **k** Ubiquitination of CD13 protein in BMMs from WT and cKO mice. **l** Measurement of CD13 degradation in BMMs from WT and cKO mice (n = 3 independent cultures). All data are presented as mean ± SEM. Statistical analysis was performed using two-tailed unpaired Student's t-test (**a**, **d**, **e**) and two-way ANOVA with Tukey post hoc test for pairwise comparisons (**l**). The experiments in **g**, **h**, and **j**, **k** were independently repeated at least three times with similar results. Source data are provided as a Source Data file.

Considering the potential interaction between UCHL1 and CD13, GROMACS was employed to elucidate the characteristics and underlying mechanisms of their interactions. Following a 100 ns molecular dynamics (MD) simulation, favorable interaction characteristics were observed without significant disruption to the proteins' structural integrity or complex compactness (Supplementary Fig. 7a–e). Energy decomposition analysis from the MD simulations guided the selection of key residues for point mutations, highlighting Asp423 and Tyr424 on CD13, and Arg153 on UCHL1 as pivotal contributors to the interaction interface. Mutating these residues to Ala resulted in a notable alteration in protein-protein interactions, with a reduction in hydrogen bonds and an increase in free binding energy (Fig. 4f, Supplementary Fig. 7a, b and Supplementary Table 2–4). The structural stability of UCHL1 Arg153Ala was compromised compared to the wild-type, as indicated by an increased RMSD scope (Supplementary Fig. 7e, f). Collectively, these simulations highlight the crucial roles of Asp423 and Tyr424 on CD13, along with Arg153 on UCHL1, in modulating the interaction between UCHL1 and CD13.

Immunoprecipitation experiments on mouse BMMs confirmed the presence of CD13 in the anti-UCHL1 immunoprecipitate but not in the immunoglobulin G (IgG) immunoprecipitate from the cell lysate (Fig. 4g). Similarly, UCHL1 was detected in the anti-CD13 immunoprecipitate, indicating the existence of an interaction between endogenous UCHL1 and CD13. Furthermore, mutations in Asp423 and Tyr424 of CD13 resulted in decreased binding to UCHL1 (Fig. 4h). The downregulated protein level of CD13 in UCHL1-deficient cells prompted us to test whether UCHL11 is a potential DUB for CD13. Protein levels and ubiquitination of CD13 in osteoarthritic subchondral bone was examined. Results indicated a notable elevation in CD13 levels within the subchondral bone of OA patients compared to non-OA individuals (Fig. 4i). Additionally, there was a decrease in ubiquitination levels of CD13 alongside an up-regulation in the expression of UCHL1 (Fig. 4j). This suggests that the augmented UCHL1 deubiquitination of CD13 leads to a reduction in ubiquitin levels and an increase in protein content. Furthermore, deletion of endogenous UCHL1 resulted in increased polyubiquitination of CD13 (Fig. 4k), explaining the reduced CD13 protein content observed in UCHL1 knockout BMMs, with mRNA expression remaining unaffected (Fig. 4e). Finally, to determine whether UCHL1 shortened the half-life of CD13 protein, we monitored the CD13 protein abundance in BMMs from WT and cKO mice after treatment with the translational inhibitor cycloheximide (CHX). In the absence of new protein synthesis, CD13 was cleared rapidly from BMMs of WT mice, with a half-life of approximately 6–9 h (Fig. 4l). Furthermore, the absence of UCHL1 was shown to significantly shorten the half-life of CD13 protein, supporting the role of UCHL1 in stabilizing CD13 protein.

UCHL1 inhibits osteoclastogenesis through the inhibitory effect of sCD13 on the MAPK signaling pathway

CD13 is a transmembrane protein that also exists in shed and secreted soluble forms (sCD13)[32]. Notably, sCD13 levels in the culture supernatant of UCHL1 knockout BMMs were decreased (Fig. 5a). To investigate the inhibitory effect of UCHL1 on osteoclastogenesis through sCD13, gain and loss of function studies are performed to causally implicate sCD13 in the effect of UCHL1 on osteoclastogenesis. UCHL1 deficiency in BMMs led to enhanced osteoclastogenesis, while recombinant adeno-associated virus, serotype 9 (rAAV9)-mediated overexpression of UCHL1 notably inhibited osteoclast formation (Fig. 5b–f). Moreover, recombinant mouse sCD13 (rsCD13) attenuated the promoting effect of UCHL1 knockout on osteoclast formation and resorption, whereas silencing of CD13 reversed the inhibitory effects of UCHL1 overexpression on osteoclasts.

Next, the effect of sCD13 on osteoclast differentiation signaling pathways was examined. RANKL mediates osteoclast differentiation and function by activating a series of signaling cascades, including the nuclear factor-kappa B (NF-κB) and mitogen-activated protein kinase (MAPK) pathways (e.g., JNK, ERK, and p38). Our findings indicated that rsCD13 effectively suppressed RANKL-induced MAPK signaling while showing no impact on NF-κB signaling (Fig. 5g, h). To further validate that the downstream effect of sCD13 is on MAPK rather than NF-κB, the ERK, P38, and JNK pathway were hyperactivated by overexpression their respective upstream kinases (i.e., MAP2K1, MAP2K6, and MAP2K7)[33,34]. Additionally, NF-κB was overactivated by ectopic expression of IKK2[34,35]. Despite these manipulations, sCD13 continued to exhibit its inhibitory effect on MAPK hyperactivation, with no impact on NF-κB hyperactivity observed (Fig. 5i). Therefore, these findings suggest that sCD13 mediates the inhibitory effect of UCHL1 on osteoclastogenesis via the MAPK signaling pathway.

UCHL1 overexpression ameliorates DMM-induced OA progression in a mouse model

Considering the role of UCHL1 in inhibiting osteoclastogenesis, it may have therapeutic implications for the treatment of OA. Adeno-associated virus (AAV) is a small, nonenveloped parvovirus measuring 26 nm in size, with a single-stranded genome approximately 4.7 kb long[36]. Its high transduction efficiency, ability to maintain transgene expression over time, and lack of post-infection immunogenicity and pathogenicity make AAV a prominent viral vector in gene therapy[37]. Two recent studies have demonstrated the effective transduction of osteoclasts in vivo using rAAV9[38,39]. In our study, we further confirmed that rAAV9 can indeed home in on osteoclasts after systemic administration (Supplementary Fig. 8a). Expanding upon this, we established an OA mouse model using the DMM method and intraperitoneally injected rAAV9-UCHL1 to induce UCHL1 overexpression in osteoclasts (Fig. 6a). rAAV9-UCHL1 injection effectively reduced osteoclast activation induced by DMM at the 2-week after surgery (Fig. 6b, c). Additionally, Micro-CT results indicated that bone volume in the subchondral bone and the thickness of the subchondral plate in the rAAV9-UCHL1 injection group were comparable to those in the sham group (Fig. 6d, e). Safranin-O/Fast Green staining and immunohistochemistry provided further support for the amelioration of DMM-induced cartilage degeneration in the group with UCHL1 overexpression in subchondral osteoclasts (Fig. 6f–i). Moreover, rAAV9-UCHL1 injection resulted in significant improvement in mechanical and thermal pain threshold at 8 weeks after DMM, as detected by the Von Frey and hot plate tests (Fig. 6j). Cysteine 90 (C90) of UCHL1 is essential for its deubiquitination activity[27,40]. In order to confirm that the protective impact of UCHL1 overexpression on OA relies on its deubiquitination activity, a catalytic mutant of UCHL1 (UCHL1C90R) was created. Results indicated that the overexpression of UCHL1C90R did not alleviate the progression of OA phenotypes induced by DMM (Supplementary Fig. 8b–k). Therefore, our findings suggest that overexpression of UCHL1 in osteoclasts through rAAV9 administration may alleviate the progression of DMM-induced OA.

Discussion

Regardless of cartilage degeneration as an important contributor, pathological osteoclastogenesis in subchondral bone has been increasingly demonstrated to be the primary trigger of OA onset and progression[11,41,42]. As a result, targeting osteoclast activity in subchondral bone has emerged as a promising therapeutic strategy for OA patients. We analyzed subchondral bone samples and observed the concurrent changes in UCHL1 expression and osteoclast activity in subchondral bone during OA progression in humans and a mouse model. Conditional deletion of UCHL1 in osteoclast precursor cells promoted osteoclastogenesis in subchondral bone and facilitated the progression of OA induced by DMM. Mechanistically, a negative feedback loop, RANKL-UCHL1-sCD13, which limits osteoclastogenesis, was identified (Fig. 6k).
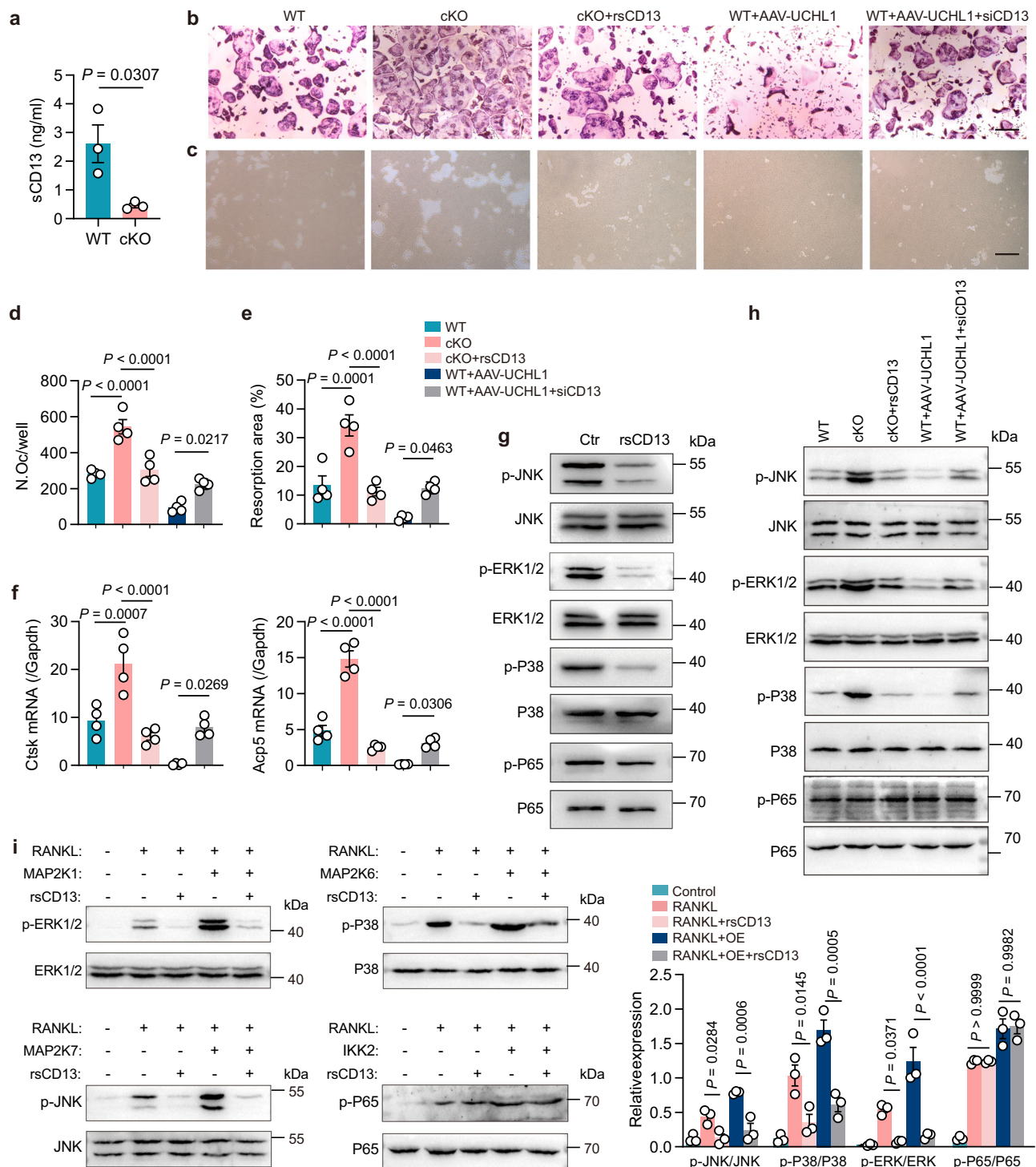
Fig. 5 | UCHL1 suppresses osteoclastogenesis via rsCD13-mediated inhibition of the MAPK signaling pathway. a Measurement of soluble CD13 (sCD13) secretion in BMM supernatants from WT and cKO mice using ELISA ($n = 3$ independent cultures). **b, c** TRAP staining and resorption analysis of BMMs from WT and cKO mice treated with overexpression AAV-UCHL1, mouse rsCD13, and siCD13. Scale bar: 200 µm. **d, e** Quantification of osteoclast number and resorption area in (**b, c**) ($n = 4$ independent cultures). **f** Quantitative real-time PCR analysis of osteoclastogenic markers in WT and cKO BMMs treated with overexpression AAV-UCHL1, mouse rsCD13, and siCD13 ($n = 4$ independent cultures). **g** Immunoblot analysis of rsCD13 on RANKL-stimulated signals in BMMs. **h** Immunoblot analysis of RANKL-

stimulated signals in BMMs from WT and cKO mice treated with overexpression AAV-UCHL1, mouse rsCD13, and siCD13. **i** Immunoblot and statistical analysis of rsCD13 on RANKL-stimulated signals in BMMs treated with MAP2K1, MAP2K6, MAP2K7, and IKK2 overexpression plasmid ($n = 3$ independent cultures). All data are presented as mean ± SEM. Statistical analysis was performed using two-tailed unpaired Student's t-test (**a**) and one-way ANOVA with Tukey post hoc test for pairwise comparisons (**d, e, f, i**). The experiments in **g, h** were independently repeated at least three times with similar results. rsCD13, recombinant sCD13; siCD13, CD13 siRNA. Source data are provided as a Source Data file.
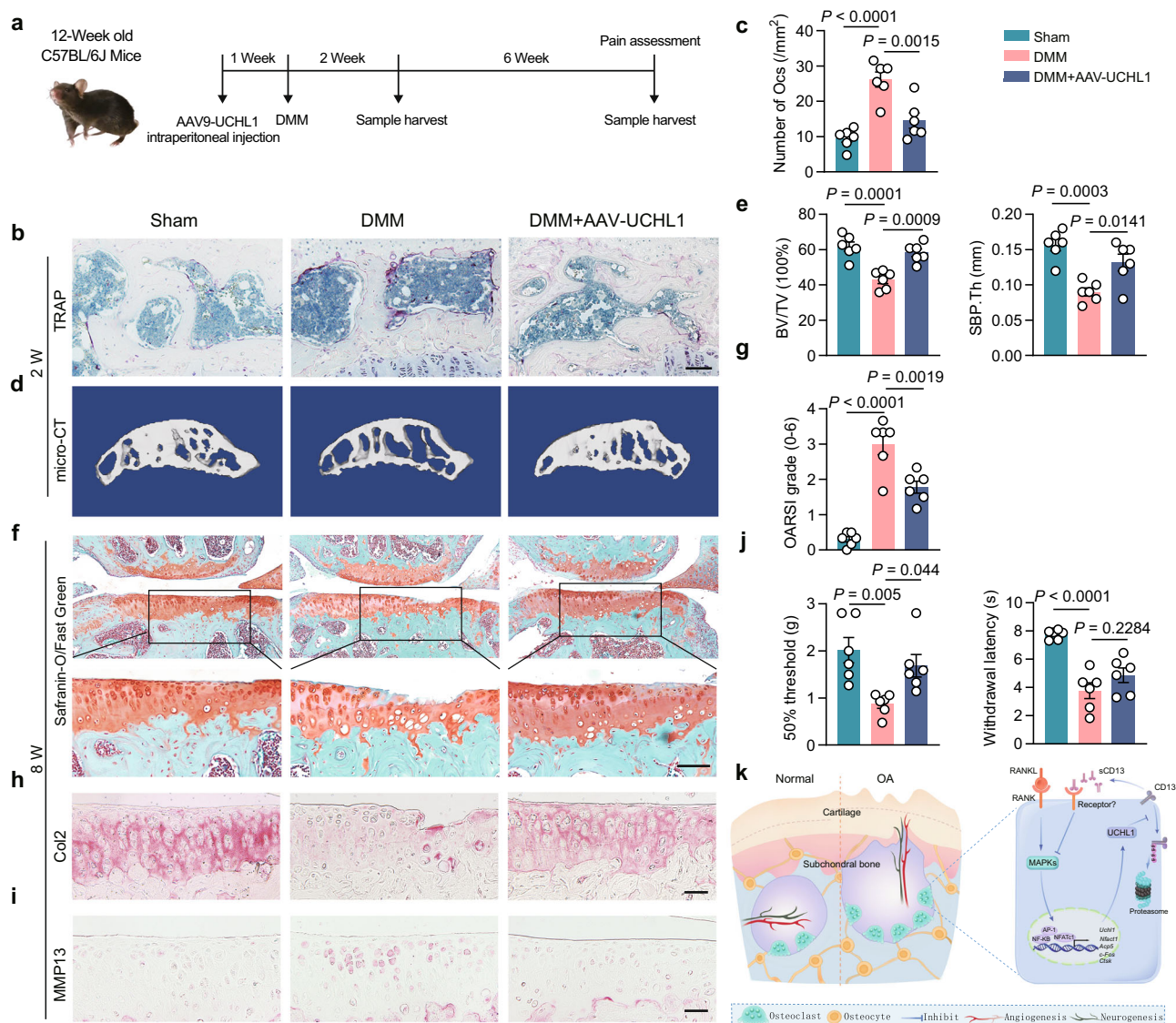
Fig. 6 | UCHL1 overexpression alleviates DMM-induced OA progression in a mouse model. a Schematic representation of the experimental design involving intraperitoneal injection of AAV9-UCHL1 into DMM mice. **b** TRAP staining of the tibia subchondral bone (coronal view) 2 weeks after DMM surgery. Scale bar: 100 μm. **c** Quantitative analysis of TRAP-positive osteoclast density in subchondral bone (*n* = 6 mice per group). **d** 3D micro-CT images of the tibial subchondral bone medial compartment 2 weeks after DMM surgery. **e** Quantitative analysis of subchondral bone volume (BV/TV) and SBP.Th (*n* = 6 mice per group). **f** Safranin-O/fast green staining of the tibial subchondral bone (coronal view) 8 weeks after DMM surgery. Scale bar: 100 μm. **g** OARSI grade of tibia articular cartilage (*n* = 6 mice per group). **h** Representative images of Col2 immunohistochemistry in tibial articular cartilage at 8 weeks after DMM. Scale bar: 50 μm. **i** Representative images of MMP13 immunohistochemistry in tibial articular cartilage at 8 weeks after DMM. Scale bar: 20 μm. **j** Paw withdrawal threshold measured in the right hind paw at 8 weeks after

DMM (*n* = 6 mice per group). **k** Schematic model of the RANKL-UCHL1-sCD13 negative feedback loop in OA development. In osteoclast precursor cells, RANKL induction leads to UCHL1 expression, subsequently stabilizing CD13, increasing sCD13 release, and triggering autocrine inhibition of the MAPK signaling pathway, thereby suppressing osteoclastogenesis. Consequently, UCHL1 deletion in pre-osteoclasts promotes osteoclastogenesis and OA progression. Conversely, UCHL1 overexpression can reverse the DMM-induced OA phenotypes. All data are presented as mean ± SEM. Statistical analysis was performed using one-way ANOVA with Tukey post hoc test for pairwise comparisons (**c, e, g, j**). The experiments in **h, i** were independently repeated six times with similar results. OA, osteoarthritis. DMM, destabilized medial meniscus; OARSI, Osteoarthritis Research Society International; BV/TV, bone volume/total volume; SBP.Th, subchondral bone plate thickness. Source data are provided as a Source Data file.

Osteoclasts, derived from hematopoietic precursor cells, undergo differentiation upon RANKL stimulation. RANKL binding to its receptor RANK triggers osteoclast precursor differentiation into mature osteoclasts[35]. Intracellular signals are transduced by RANK through adapter molecules such as TRAF6, subsequently activating MAPK and NF-κB, leading to the transcription of osteoclast genes[43]. Negative feedback loops are often incorporated into homeostatic signaling pathways, wherein a transcription factor triggers the expression of an upstream negative regulator[44]. RANKL-signaling pathways induce several negative regulators to restrain excessive

osteoclast activation. An exemplar of this is IFNβ[45], where RANKL induces IFNβ expression, which then binds to its receptors and transmits inhibitory signals to suppress RANKL-induced c-Fos expression. Our findings revealed that RANKL induces UCHL1 expression during osteoclastogenesis. Acting as a deubiquitinating enzyme, UCHL1 stabilizes CD13, resulting in increased secretion of sCD13. This autocrine action of increased sCD13 acts on osteoclast precursor cells and inhibits RANKL-induced MAPK activation, thereby impeding osteoclast differentiation. The RANKL-UCHL1-sCD13 negative feedback loop fine-tunes osteoclastogenesis, and UCHL1

deficiency in osteoclast precursor cells disrupts this feedback loop, promoting osteoclast formation.

Deubiquitinating enzymes, extensively studied in the field of bone biology, include OTUB1[46], USP26[47], USP34[48], USP1[49], and Cyld[50]. UCHL1 was recently found to negatively regulate osteoclastogenesis and osteoporosis progression[30]. Our findings indicated that knockout UCHL1 does not impact the OA phenotypes in mice under normal physiological conditions. However, UCHL1 expression is upregulated in subchondral bone in DMM-induced OA mouse model and OA patients. While elevated UCHL1 levels are linked to increased osteoclast activity in OA, UCHL1 itself actually inhibits osteoclastogenesis. This paradoxical relationship suggests that the body may be attempting to compensate for the excessive osteoclast activity that contributes to OA by increasing UCHL1 production. However, this mechanism may not be sufficient or effective enough under the diseased conditions. Consequently, enhancing the function or activity of UCHL1 could potentially restore the balance of bone metabolism, thereby mitigating the progression of OA through the reduction of excessive bone resorption. A similar pattern was observed in a recent study[30] where UCHL1 expression was upregulated in the metaphysis of OVX mice, yet knockout of UCHL1 did not impact bone mass in mice under normal physiological conditions. In contrast, the bone mass of UCHL1 knockout mice under OVX conditions was notably reduced, and UCHL1 overexpression protected against this bone loss.

Excessive subchondral bone remodeling, triggered by heightened osteoclastic bone resorption, is considered the primary pathological characteristic of early-stage OA[11–13]. Both our findings and those of other researchers demonstrate a significant increase in TRAP-positive osteoclasts in subchondral bone following the application of an OA model[14,51]. This increase peaks at 2 weeks after DMM surgery, coinciding with the most pronounced subchondral bone resorption and subsequent decrease in subchondral bone content. Notably, articular cartilage degeneration is not yet observed at this stage, only becoming apparent at 4 weeks after DMM. As a result, changes in subchondral bone microstructure resulting from heightened osteoclast activity occur prior to the onset of cartilage degeneration. Thus, targeting osteoclasts with drugs holds promise as a therapeutic strategy for OA treatment. Preclinical experimental studies and clinical trials have demonstrated the beneficial effect of inhibiting osteoclast function using bisphosphonates or MIV-711, an inhibitor of cathepsin K, on OA[16,21,22,52,53]. In this study, UCHL1 deletion in osteoclast precursor cells significantly worsened various parameters associated with OA progression, including subchondral bone microarchitecture and cartilage destruction. Conversely, the overexpression of UCHL1 using AAV9 reversed the OA phenotypes induced by DMM. Therefore, the overexpression of UCHL1 represents a potential target for intervening in OA.

In summary, we identify a negative feedback loop, RANKL-UCHL1-sCD13, which limits osteoclast differentiation. Deletion of UCHL1 in osteoclast precursor cells leads to elevated subchondral osteoclastogenesis, abnormal subchondral bone remodeling, and exacerbated OA progression, while overexpression of UCHL1 through adeno-associated virus serotype 9 alleviates these processes. Thus, our results suggest that RANKL-UCHL1-sCD13 negative feedback loop is essential for the joint to maintain healthy homeostasis and prevent OA progression.

Methods
Ethics statement
Our research complies with all relevant ethical regulations. The study received approval from the Ethics Committee of Zhujiang Hospital, Southern Medical University (2019KY02203). Written informed consents were obtained from the patients. The animal care protocols and

experiments were reviewed and approved by the Animal Ethics Committee of Zhujiang Hospital of Southern Medical University (LAEC2021123).

Mice
C57BL/6 J mice were obtained from the Laboratory Animal Centre of Southern Medical University. UCHL1$^{fl/fl}$ mice on C57BL/6 J background were generated by floxing exon 4 in the UCHL1 allele using a Cas9-CRISPR workflow provided by GemPharmatech. LysM-Cre transgenic mice on C57BL/6 J background were purchased from GemPharmatech and crossed with UCHL1$^{fl/fl}$ mice. Mouse genotypes were determined by PCR analysis of tail genomic DNA using the primers listed in Supplementary Table 5. All mice analyzed were bred and maintained on the C57BL/6 J background. They were housed in a controlled environment with a temperature range of 20–26 °C and humidity levels between 40 and 70%, under a 12-hour light/dark cycle. These mice were fed an irradiated chow diet (#1035 for reproductive feeding and #1025 for maintenance feeding, Beijing HFK Bioscience Co., Ltd, Beijing, China) and had free access to drinking water. All animal experiments complied with the ARRIVE guidelines for reporting animal experiments. Euthanasia was performed by cervical dislocation under deep anesthesia.

Human samples
Non-OA subchondral bone samples were obtained from three individuals with no history of OA. OA subchondral bone samples were collected from five patients who underwent total knee arthroplasty at Zhujiang Hospital of Southern Medical University. All individuals who participated in the experiment were aware of the use of their samples and provided their written informed consent. No compensation was given. Clinical characteristics of the patients are detailed in Supplementary Table 1.

Deubiquitinase gene microarray
Gene expression profiles were analyzed using the human deubiquitinase PCR array according to the manufacturer's protocol (Wcgene Biotech, Shanghai, China). Data were analyzed using Wcgene Biotech software. Genes with fold-changes >2 and p < 0.05 were considered to be biological significant.

Mouse model of DMM-induced OA
In the study, only male mice were chosen for this experiment due to the higher incidence of post-traumatic osteoarthritis models in male mice compared to female mice in mouse studies[54]. Female hormones exhibit protective effects on cartilage, whereas male hormones can worsen cartilage conditions[55]. Post-traumatic OA was induced by DMM surgery as previously described[56]. Briefly, 12-week-old male mice were anesthetized with tribromoethanol, and aseptic surgery was performed on their right knees. After making a medial parapatellar arthrotomy, the anterior fat pad was dissected to expose the anterior medial meniscotibial ligament, which was then severed. The knee was flushed with saline solution, and the incision was closed. In the case of sham-surgery animals, the joint capsule was opened without cutting the meniscotibial ligament. The knees of the animals were examined at 2- and 8-weeks post-surgery. The subchondral bone microstructure was evaluated using micro-computed tomography, while the degree of cartilage destruction in the knee joints was assessed through safranin O staining and scored according to the OARSI grading system.

rAAV9 injection
Recombinant adeno-associated virus serotype 9 expressing UCHL1 (AAV9-UCHL1) and C90-mutated UCHL1 (UCHL1C90R) were prepared by OBiO Technology (Shanghai, China). A single dose of 5×10^{11} virus

was administered to C57BL/6 J mice with DMM-induced OA by intra-peritoneal injection 1 week before surgery. Mice were sacrificed at 2 weeks and 8 weeks post-surgery for histological analyzes.

Behavioral assessment

Quantification of mechanical and thermal allodynia was conducted by an unbiased observer who was unaware of any treatments administered. Mice were placed in transparent cubicles on a perforated metal floor and allowed to acclimate for at least 10 min before testing. Paw withdrawal thresholds in response to mechanical stimuli were assessed using the up–down testing paradigm with Von Frey monofilaments (Semmes–Weinstein), as previously described[57,58]. The 50% paw withdrawal thresholds were determined by applying the up–down method of Dixon to the pattern of positive and negative withdrawal responses[57].

The plantar test was conducted using radiant heating (IITC 390 G Plantar Test; IITC Life Science, Woodland Hills, CA). In this test, the hind paw of each mouse was stimulated with an infrared light beam source to elicit noxious withdrawal responses[59]. The time it took for the paw to withdraw in response to the infrared light stimulation was measured. Each mouse underwent 3 trials with their right hind paws, and there was a 5-minute break between each trial. The withdrawal latency was determined by averaging the values obtained from each paw.

Micro-CT analysis

Subchondral bone changes after DMM surgery were evaluated using micro-CT scanning. The tibias were dissected from mice, and the attached muscle was carefully removed. The tissues were then fixed with 4% paraformaldehyde for 48 hours. Micro-CT analysis was performed using a micro-computed tomography system (μCT 40 scanner, Scano Medical, Switzerland) at a resolution of 10 μm, with 55-kVp energy, 145-μA intensity, and 200 ms integration time. A subsection (0.5 mm medio-lateral width, 1.0 mm ventro-dorsal length) of the load-bearing region of the subchondral bone was taken as region of interest. The Scanco analysis software was used to analyze the subchondral bone volume/total volume (BV/TV, %) and subchondral bone plate thickness of the medial tibial subchondral bones. Finally, a total of five consecutive cross-sectional images from medial tibial plateau was used for 3D reconstruction using Mimics software (Mimics Research 21.0, Materialize, Belgium).

Histological analysis and immunostaining

The cartilages were fixed, embedded in paraffin, and cut into 4 μm sections. These sections were deparaffinized, hydrated, and stained with Safranin-O/fast green, Hematoxylin/eosin (HE), and TRAP staining. The severity of cartilage damage was assessed using the Osteoarthritis Research Society International (OARSI) scoring system. The OARSI grades of the medial tibia were assessed by averaging the scores of three experienced investigators. For the immunostaining assay, the sections were incubated with primary antibodies overnight at 4 °C, followed by incubation with secondary antibodies at room temperature. The antibodies used for immunostaining are listed in Supplementary Table 6.

Osteoclastogenesis and resorption assay

BMMs were obtained by flushing long bones from adult mice and cultured as previously described[60]. To generate osteoclasts, BMMs were plated onto 96-well plates at a density of 1×10^4 cells/well. The BMMs were cultured with α-MEM medium supplemented with M-CSF (20 ng/ml) and RANKL (50 ng/ml) for 5 days. TRAP staining was performed according to a protocol provided by Sigma-Aldrich. Osteoclasts were identified as TRAP-positive cells containing three or more nuclei, using bright-field light microscopy. For the bone resorption assay, BMMs were placed onto 96-well Corning osteo assay surface at a density of 1×10^4 cells/well. The BMMs were cultured with α-MEM medium supplemented with M-CSF (20 ng/ml) and RANKL (50 ng/ml). Cell culture media were replaced every 2 days until mature osteoclasts had formed. After 10 days, the osteoclasts were removed from the surface using hypochlorous acid. The percentage of resorbed bone surface area was quantified using Image J software.

Western blot

Western blot analysis was conducted as previously described[61]. Whole-cell lysates were generated by lysing cells using RIPA Lysis Buffer with Protease Inhibitor Cocktail (Roche4693132001). The lysates were clarified by centrifugation, quantified using the BCA assay, and mixed with dual color protein loading buffer (Fdbio science FD002). The resulting mixture was separated by SDS-PAGE and transferred to a PVDF membrane. Membranes were incubated in blocking buffer, followed by incubation with the primary antibody at 4 °C. After washing, the membranes were incubated with an enzyme-labeled secondary antibody. Finally, the membranes were washed and subjected to autoradiography. The antibodies used for western blot are listed in Supplementary Table 6.

Immunoprecipitation analysis

Cells were treated with lysis buffer containing 1% NP-40, 25 mM Tris-HCl (pH 7.4), 150 mM NaCl, 1 mM EDTA, and a protease inhibitor cocktail (Roche) for 20 min at 4 °C. The mixture was then centrifuged at 12,000 g for 15 min at 4 °C. For immunoprecipitation, approximately 500 μg of protein was combined with either control or specific antibodies (2–4 μg) and left to incubate overnight at 4 °C with constant rotation. Subsequently, 50 μl of Protein A/G magnetic beads (Selleck) were added, followed by an additional 15-minute incubation. The beads were washed five times using the lysis buffer, with collection by magnetic stand at 4 °C between washes. The proteins were eluted from the beads by resuspending them in 2× SDS-PAGE loading buffer and boiling for 5 min. The resulting immune complexes were then analyzed by SDS-PAGE and immunoblotting using appropriate antibodies.

In vivo ubiquitination assay

All ubiquitin immunoprecipitation was conducted under denaturing conditions. Prior to sample collection, cells were treated with 20 μM of the proteasome inhibitor MG132 for 6 h. Cells or tissues were lysed in 1% sodium dodecyl sulfate (SDS), followed by boiling and sonication, before dilution in RIPA lysis buffer (comprising 25 mM Tris-HCl pH 7.6, 150 mM NaCl, 1 mM EDTA, 1% NP40, 1% sodium deoxycholate, and 0.1% SDS). The lysates were then immunoprecipitated using an anti-CD13 antibody. The resulting immunoprecipitates underwent five washes with RIPA buffer and were subsequently analyzed via immunoblotting with anti-Ub.

Real-time quantitative PCR

Total RNA was extracted from cells or tissues using TRIzol Reagent (9109 RNAiso Plus Takara). Cells or tissue powder were collected, resuspended in 1 mL TRIzol, and lysed at room temperature for 10 min. Chloroform (0.2 mL per 1 mL of TRIzol) was added, mixed well, and incubated for 5 min. After centrifugation at 4 °C, the collected supernatant was mixed with 0.5 mL isopropanol for 5 min at room temperature to extract RNA. Finally, the RNA pellet was dissolved in 50 μL of nuclease-free water. RNA quality and quantity were determined using a nanodroplet spectrophotometer (Thermo Fisher Scientific, Waltham, MA, USA). RNA was reverse transcribed using PrimeScript™ RT Master Mix (Takara RR036Q). qPCR detection was performed using ChamQ SYBR qPCR Master Mix (Vazyme, Q311-02). In all qPCR experiments, 3–4 biological replicates were used, where each replicate represents an independent RNA extraction from a separate cell culture or human sample. For each biological replicate, two technical

replicates were performed to ensure the reliability of the qPCR measurements. The primers used for qPCR are listed in Supplementary Table 5.

Cell proliferation assay

Cell proliferation was assessed using the BeyoClick™ EdU Cell Proliferation Kit with Alexa Fluor 555 (Beyotime, C0075S), following the manufacturer's instructions. Briefly, cells were incubated with 10 μM EdU at 37 °C, 5% CO_2 for 2 h. After fixation with 4% paraformaldehyde for 15 min at room temperature, cells were stained with Alexa Fluor 555 reaction mixture for 30 min and Hoechst 33342 for 10 min. Immunocytochemical analysis was then performed to examine the cells. EdU-positive cells were identified by staining with Alexa Fluor 555 and Hoechst 33342. Images were captured from five randomly selected fields of view using an Olympus IX53 fluorescence microscope (Olympus, Japan). The percentage of EdU+ cells was computed for further analysis of the cells.

Molecular docking

Docking simulations between CD13 and UCHL1 were performed using the GRAMM Web Server database ((https://gramm.compbio.ku.edu/)). Initial models of CD13 and UCHL1 were retrieved from the Protein Data Bank (PDB ID: 5LHD for CD13 and 2ETL for UCHL1, https://www.rcsb.org/). Structural visualization was done using PyMOL, UCSF Chimera, and UCSF ChimeraX. Point mutations and energy minimization were carried out using UCSF Chimera.

Molecular dynamics simulations were conducted using Gromacs2022.3 software[62]. The simulations were run at 300 K and 1 Bar pressure. The Amber99sb-ildn force field was applied to the proteins, while Tip3p water model was used for the solvent. Neutralization of the system's total charge was achieved by adding Na + ions. Energy minimization was performed using the steepest descent method. Equilibrium simulations were conducted under both isothermal isovolumic and isothermal isobaric ensembles. Subsequently, free molecular dynamics simulations were run for 100 ns. Trajectory analysis included RMSD, RMSF, SASA, and protein rotation radius. Free energy binding was estimated through MM/PBSA calculations.

Proteomics analysis

Three independent cultures of BMMs were collected from WT and cKO mice, respectively. The 4D label-free quantitative proteomics analysis was performed by Jingjie PTM BioLab (Hangzhou) Co. Inc. For protein extraction, cells were lysed with lysis buffer (8 M urea, 1% protease inhibitor cocktail) on ice for 30 min, followed by centrifugation (12,000 g, 10 min, and 4 °C). The supernatant was collected and the protein concentration was determined with BCA kit according to the manufacturer's instructions.

For digestion, the sample was slowly added to the final concentration of 20% (m/v) TCA to precipitate protein, then vortexed to mix and incubated for 2 h at 4 °C. The precipitate was collected by centrifugation at 4500 g for 5 min at 4 °C. The precipitated protein was washed with pre-cooled acetone for 3 times and dried for 1 min. The protein sample was then redissolved in 200 mM TEAB and ultrasonically dispersed. Trypsin was added at 1:50 trypsin-to-protein mass ratio for the first digestion overnight. The sample was reduced with 5 mM dithiothreitol for 60 min at 37 °C and alkylated with 11 mM iodoacetamide for 45 min at room temperature in darkness. Finally, the peptides were desalted by Strata X SPE column.

For LC-MS/MS analysis, the tryptic peptides were dissolved in solvent A (0.1% formic acid, 2% acetonitrile in water), directly loaded onto a home-made reversed-phase analytical column (25-cm length, 100 um i.d.). Peptides were separated with a gradient from 6% to 24% solvent B (0.1% formic acid in acetonitrile) over 70 min, 24% to 32% in 14 min and climbing to 80% in 3 min then holding at 80% for the last 3 min, all at a constant flow rate of 450 nL/min on a nanoElute UHPLC system (Bruker Daltonics).

The peptides were subjected to Capillary source followed by the timsTOF Pro (Bruker Daltonics) mass spectrometry. The electrospray voltage applied was 1.70 kV. Precursors and fragments were analyzed at the TOF detector (a MS/MS scan range from 100 to 1700 m/z). The timsTOF Pro was operated in parallel accumulation serial fragmentation (PASEF) mode. Precursors with charge states 0 to 5 were selected for fragmentation, and 10 PASEF-MS/MS scans were acquired per cycle. The dynamic exclusion was set to 30 s.

For database search, the resulting MS/MS data were processed using MaxQuant search engine (v.1.6.15.0). Tandem mass spectra were searched against the Mus_musculus_10090_SP_20201214.fasta (17063 entries) concatenated with reverse decoy database. Trypsin/P was specified as cleavage enzyme allowing up to 2 missing cleavages. Min. peptide length was set as 7 and max. number of modification per peptide was set as 5. The mass tolerance for precursor ions was set as 20 ppm in First search and 20 ppm in Main search, and the mass tolerance for fragment ions was set as 0.02 Da. Carbamidomethyl on Cys was specified as fixed modification, and acetylation on protein N-terminal and oxidation on Met were specified as variable modifications. False discovery rate (FDR) of protein, peptide and PSM was adjusted to <1%.

Statistical analysis

Each experiment was repeated at least three times. Biological replicates are samples from different biological sources or units, while technical replicates are repeated measurements of the same sample under the same conditions. The data are presented as mean ± SEM. We employed unpaired, two-tailed Student's t-test for comparisons between two groups and ANOVA with Tukey post hoc test for multiple comparisons. A significance level of $P < 0.05$ was considered statistically significant. Graphs and statistical analyzes were generated using GraphPad Prism 9.0 software.

Reporting summary

Further information on research design is available in the Nature Portfolio Reporting Summary linked to this article.

Data availability

All data generated or analyzed during this study are included in this published article (and its supplementary information files). The mass spectrometry proteomics data generated in this study have been deposited to the ProteomeXchange Consortium database: PXD052578 (https://proteomecentral.proteomexchange.org) via the iProX partner repository[63,64]. Source data are provided with this paper.

References

1. Hunter, D. J. & Bierma-Zeinstra, S. Osteoarthritis. *The Lancet* **393**, 1745–1759 (2019).
2. Disease, G. B. D., Injury, I. & Prevalence, C. Global, regional, and national incidence, prevalence, and years lived with disability for 354 diseases and injuries for 195 countries and territories, 1990-2017: a systematic analysis for the Global Burden of Disease Study 2017. *Lancet* **392**, 1789–1858 (2018).
3. Latourte, A., Kloppenburg, M. & Richette, P. Emerging pharmaceutical therapies for osteoarthritis. *Nature reviews. Rheumatology* **16**, 673–688 (2020).
4. Reichenbach, S. et al. Effect of biomechanical footwear on knee pain in people with knee osteoarthritis: the BIOTOK randomized clinical trial. *Jama* **323**, 1802–1812 (2020).
5. Katz, J. N., Arant, K. R. & Loeser, R. F. Diagnosis and treatment of hip and knee osteoarthritis: a review. *Jama* **325**, 568–578 (2021).
6. Lotz, M. K. & Caramés, B. Autophagy and cartilage homeostasis mechanisms in joint health, aging and OA. *Nature reviews. Rheumatology* **7**, 579–587 (2011).

7. Yao, Q. et al. Osteoarthritis: pathogenic signaling pathways and therapeutic targets. *Signal Transduct Target Ther* **8**, 56 (2023).

8. Zhang, H., Cai, D. & Bai, X. Macrophages regulate the progression of osteoarthritis. *Osteoarthritis and cartilage* https://doi.org/10.1016/j.joca.2020.01.007 (2020).

9. Vincent, T. L. et al. Osteoarthritis pathophysiology: therapeutic target discovery may require a multifaceted approach. *Clin Geriatr Med* **38**, 193–219 (2022).

10. Mazur, C. M. et al. Osteocyte dysfunction promotes osteoarthritis through MMP13-dependent suppression of subchondral bone homeostasis. *Bone Research* **7**, 34 (2019).

11. Hu, W., Chen, Y., Dou, C. & Dong, S. Microenvironment in subchondral bone: predominant regulator for the treatment of osteoarthritis. *Annals of the rheumatic diseases* https://doi.org/10.1136/annrheumdis-2020-218089 (2020).

12. Hu, Y., Chen, X., Wang, S., Jing, Y. & Su, J. Subchondral bone microenvironment in osteoarthritis and pain. *Bone Res* **9**, 20 (2021).

13. Li, G. et al. Subchondral bone in osteoarthritis: insight into risk factors and microstructural changes. *Arthritis research & therapy* **15**, 223 (2013).

14. Zhu, S. et al. Subchondral bone osteoclasts induce sensory innervation and osteoarthritis pain. *J Clin Invest* https://doi.org/10.1172/JCI121561 (2018).

15. Xu, L. et al. Early zoledronate treatment inhibits subchondral bone microstructural changes in skeletally-mature, ACL-transected canine knees. *Bone* **167**, 116638 (2023).

16. Ziemian, S. N., Witkowski, A. M., Wright, T. M., Otero, M. & van der Meulen, M. C. H. Early inhibition of subchondral bone remodeling slows load-induced posttraumatic osteoarthritis development in mice. *Journal of bone and mineral research: the official journal of the American Society for Bone and Mineral Research* **36**, 2027–2038 (2021).

17. Neogi, T., Li, S., Peloquin, C., Misra, D. & Zhang, Y. Effect of bisphosphonates on knee replacement surgery. *Annals of the rheumatic diseases* **77**, 92–97 (2018).

18. Laslett, L. L., Kingsbury, S. R., Hensor, E. M., Bowes, M. A. & Conaghan, P. G. Effect of bisphosphonate use in patients with symptomatic and radiographic knee osteoarthritis: data from the Osteoarthritis Initiative. *Annals of the rheumatic diseases* **73**, 824–830 (2014).

19. Kadri, A. et al. Inhibition of bone resorption blunts osteoarthritis in mice with high bone remodelling. *Annals of the rheumatic diseases* **69**, 1533–1538 (2010).

20. Bihlet, A. R. et al. Symptomatic and structural benefit of cathepsin K inhibition by MIV-711 in a subgroup with unilateral pain: post-hoc analysis of a randomised phase 2a clinical trial. *Clin Exp Rheumatol* **40**, 1034–1037 (2022).

21. Conaghan, P. G. et al. Disease-modifying effects of a novel cathepsin k inhibitor in osteoarthritis: a randomized controlled trial. *Ann Intern Med* **172**, 86–95 (2020).

22. Lindstrom, E. et al. The selective cathepsin K inhibitor MIV-711 attenuates joint pathology in experimental animal models of osteoarthritis. *Journal of translational medicine* **16**, 56 (2018).

23. Wittoek, R., Verbruggen, G., Vanhaverbeke, T., Colman, R. & Elewaut, D. RANKL blockade for erosive hand osteoarthritis: a randomized placebo-controlled phase 2a trial. *Nature medicine* https://doi.org/10.1038/s41591-024-02822-0 (2024).

24. Todi, S. V. & Paulson, H. L. Balancing act: deubiquitinating enzymes in the nervous system. *Trends in neurosciences* **34**, 370–382 (2011).

25. Reichelt, J. et al. Non-functional ubiquitin C-terminal hydrolase L1 drives podocyte injury through impairing proteasomes in autoimmune glomerulonephritis. *Nature communications* **14**, 2114 (2023).

26. Geng, B. et al. UCHL1 protects against ischemic heart injury via activating HIF-1alpha signal pathway. *Redox Biol* **52**, 102295 (2022).

27. Bi, H.-L. et al. The deubiquitinase UCHL1 regulates cardiac hypertrophy by stabilizing epidermal growth factor receptor. *Science Advances* **6**, eaax4826 (2020).

28. Shim, S., Kwon, Y. B., Yoshikawa, Y. & Kwon, J. Ubiquitin C-terminal hydrolase L1 deficiency decreases bone mineralization. *J Vet Med Sci* **70**, 649–651 (2008).

29. Coudert, A. E. et al. Differentially expressed genes in autosomal dominant osteopetrosis type II osteoclasts reveal known and novel pathways for osteoclast biology. *Lab Invest* **94**, 275–285 (2014).

30. Feng, Z. et al. The deubiquitinase UCHL1 negatively controls osteoclastogenesis by regulating TAZ/NFATC1 signalling. *International journal of biological sciences* **19**, 2319–2332 (2023).

31. Naito, A. T. et al. Complement C1q activates canonical Wnt signaling and promotes aging-related phenotypes. *Cell* **149**, 1298–1313 (2012).

32. Tsou, P. S. *et al*. Soluble CD13 induces inflammatory arthritis by activating the bradykinin receptor B1. *J Clin Invest* **132**, https://doi.org/10.1172/JCI151827 (2022).

33. Arthur, J. S. & Ley, S. C. Mitogen-activated protein kinases in innate immunity. *Nat Rev Immunol* **13**, 679–692 (2013).

34. Oeckinghaus, A. & Ghosh, S. The NF-kappaB family of transcription factors and its regulation. *Cold Spring Harb Perspect Biol* **1**, a000034 (2009).

35. Boyle, W. J., Simonet, W. S. & Lacey, D. L. Osteoclast differentiation and activation. *Nature* **423**, 337–342 (2003).

36. Rose, J. A., Hoggan, M. D. & Shatkin, A. J. Nucleic acid from an adeno-associated virus: chemical and physical studies. *Proceedings of the National Academy of Sciences of the United States of America* **56**, 86–92 (1966).

37. Vandenberghe, L. H., Wilson, J. M. & Gao, G. Tailoring the AAV vector capsid for gene therapy. *Gene Therapy* **16**, 311–319 (2009).

38. Yang, Y. S. et al. Bone-targeting AAV-mediated gene silencing in osteoclasts for osteoporosis therapy. *Mol Ther Methods Clin Dev* **17**, 922–935 (2020).

39. John, A. A. et al. AAV-mediated delivery of osteoblast/osteoclast-regulating miRNAs for osteoporosis therapy. *Mol Ther Nucleic Acids* **29**, 296–311 (2022).

40. Gong, B. et al. Ubiquitin hydrolase Uch-L1 rescues beta-amyloid-induced decreases in synaptic function and contextual memory. *Cell* **126**, 775–788 (2006).

41. Bertuglia, A. et al. Osteoclasts are recruited to the subchondral bone in naturally occurring post-traumatic equine carpal osteoarthritis and may contribute to cartilage degradation. *Osteoarthritis and cartilage* **24**, 555–566 (2016).

42. Aso, K. et al. Associations of Symptomatic Knee Osteoarthritis With Histopathologic Features in Subchondral Bone. *Arthritis Rheumatol* **71**, 916–924 (2019).

43. Edwards, J. R. & Mundy, G. R. Advances in osteoclast biology: old findings and new insights from mouse models. *Nature reviews. Rheumatology* **7**, 235–243 (2011).

44. Yosef, N. & Regev, A. Impulse control: temporal dynamics in gene transcription. *Cell* **144**, 886–896 (2011).

45. Takayanagi, H. et al. RANKL maintains bone homeostasis through c-Fos-dependent induction of interferon-beta. *Nature* **416**, 744–749 (2002).

46. Zhu, Q. et al. OTUB1 promotes osteoblastic bone formation through stabilizing FGFR2. *Signal Transduct Target Ther* **8**, 142 (2023).

47. Li, C. et al. The osteoprotective role of USP26 in coordinating bone formation and resorption. *Cell Death Differ* **29**, 1123–1136 (2022).

48. Guo, Y. C. et al. Ubiquitin-specific protease USP34 controls osteogenic differentiation and bone formation by regulating BMP2 signaling. *EMBO J* **37**, https://doi.org/10.15252/embj.201899398 (2018).

49. Williams, S. A. et al. USP1 deubiquitates ID proteins to preserve a mesenchymal stem cell program in osteosarcoma. *Cell* **146**, 918–930 (2011).

50. Jin, W. et al. Deubiquitinating enzyme CYLD negatively regulates RANK signaling and osteoclastogenesis in mice. *J Clin Invest* **118**, 1858–1866 (2008).

51. Zhang, H. et al. Maintaining hypoxia environment of subchondral bone alleviates osteoarthritis progression. *Sci Adv* **9**, eabo7868 (2023).

52. Strassle, B. W. et al. Inhibition of osteoclasts prevents cartilage loss and pain in a rat model of degenerative joint disease. *Osteoarthritis and cartilage* **18**, 1319–1328 (2010).

53. Mohan, G. et al. Pre-emptive, early, and delayed alendronate treatment in a rat model of knee osteoarthritis: effect on sub-chondral trabecular bone microarchitecture and cartilage degradation of the tibia, bone/cartilage turnover, and joint discomfort. *Osteoarthritis and cartilage* **21**, 1595–1604 (2013).

54. van der Kraan, P. M. Factors that influence outcome in experimental osteoarthritis. *Osteoarthritis and cartilage* **25**, 369–375 (2017).

55. Ma, H. L. et al. Osteoarthritis severity is sex dependent in a surgical mouse model. *Osteoarthritis and cartilage* **15**, 695–700 (2007).

56. Glasson, S. S., Blanchet, T. J. & Morris, E. A. The surgical destabilization of the medial meniscus (DMM) model of osteoarthritis in the 129/SvEv mouse. *Osteoarthritis and cartilage* **15**, 1061–1069 (2007).

57. Chaplan, S. R., Bach, F. W., Pogrel, J. W., Chung, J. M. & Yaksh, T. L. Quantitative assessment of tactile allodynia in the rat paw. *J Neurosci Methods* **53**, 55–63 (1994).

58. Gonzalez-Cano, R. et al. Up-down reader: an open source program for efficiently processing 50% von Frey thresholds. *Front Pharmacol* **9**, 433 (2018).

59. Hargreaves, K., Dubner, R., Brown, F., Flores, C. & Joris, J. A new and sensitive method for measuring thermal nociception in cutaneous hyperalgesia. *Pain* **32**, 77–88 (1988).

60. Liang, W. et al. Skin chronological aging drives age-related bone loss via secretion of cystatin-A. *Nature Aging* https://doi.org/10.1038/s43587-022-00285-x (2022).

61. Liang, W. et al. An integrated multi-omics analysis reveals osteo-kines involved in global regulation. *Cell Metabolism* https://doi.org/10.1016/j.cmet.2024.03.006 (2024).

62. Abraham, M. J. et al. GROMACS: High performance molecular simulations through multi-level parallelism from laptops to super-computers. *SoftwareX* **1-2**, 19–25 (2015).

63. Chen, T. et al. iProX in 2021: connecting proteomics data sharing with big data. *Nucleic Acids Research* **50**, D1522–D1527 (2022).

64. Ma, J. et al. iProX: an integrated proteome resource. *Nucleic Acids Research* **47**, D1211–D1217 (2019).

Acknowledgements

Author contributions

T.Y.C., Z.P.Z., W.Q.L., and B.H designed the study. W.Q.L., R.F., X.J.L. and X.W.D conducted most of the assays and analyzed the data. S.R.F. conducted the docking model. X.J.L., J.C., and Y.C.L. assisted with animal housing and genotype identification. J.Q.C., Z.Z.L., S.A.T., and X.G.W. participated in some experiments and collected human samples. T.Y.C. drafted the manuscript and supervised the work. G.F.R. and C.H.D. revised the manuscript. W.Q.L., R.F., X.J.L. and X.W.D. contributed equally to this work. All authors approved the final version of the manuscript. T.Y.C. took full responsibility for the finished work, had access to the data, and controlled the decision to publish.

Competing interests

The authors declare no competing interests.

Additional information

Supplementary information The online version contains supplementary material available at https://doi.org/10.1038/s41467-024-53119-2.

Correspondence and requests for materials should be addressed to Wenquan Liang, Bin Huang, Zhipeng Zou or Tianyu Chen.

Peer review information *Nature Communications* thanks Jarred Whitlock, and the other, anonymous, reviewer(s) for their contribution to the peer review of this work. A peer review file is available.

Reprints and permissions information is available at http://www.nature.com/reprints

Publisher's note Springer Nature remains neutral with regard to jurisdictional claims in published maps and institutional affiliations.